Using Interaction-Based Readouts to Approach the Ultimate Limit of Detection Noise Robustness for Quantum-Enhanced Metrology in Collective Spin Systems.

Simon A. Haine[1, 2, *]

[1] *Department of Physics and Astronomy, University of Sussex, Brighton BN1 9QH, United Kingdom*
[2] *Department of Quantum Science, Australian National University, Canberra, Australia*

We consider the role of detection noise in quantum-enhanced metrology in collective spin systems, and derive a fundamental bound for the maximum obtainable sensitivity for a given level of added detection noise. We then present an interaction-based readout utilising the commonly used one-axis twisting scheme that approaches this bound for states generated via several commonly considered methods of generating quantum enhancement, such as one-axis twisting, two-axis counter-twisting, twist-and-turn squeezing, quantum non-demolition measurements, and adiabatically scanning through a quantum phase transition. We demonstrate that our method performs significantly better than other recently proposed interaction-based readouts. These results may help provide improved sensitivity for quantum sensing devices in the presence of unavoidable detection noise.

arXiv:1806.00057v2 [quant-ph] 29 Sep 2018

There is a continued push for improved metrological potential in devices such as atomic clocks, atomic magnetometers, and inertial sensors based on atom interferometry [1]. The physics of these systems is well described by collective spin-systems [2]. Over the last decade there has been rapid progress in the demonstration of quantum enhanced metrology in these systems, that is, parameter estimation with sensitivity surpassing the shot-noise limit (SNL) [3–19]. These schemes generally require a state preparation step, where inter-particle entanglement is created to enhance the metrological potential [20–22], before the classical parameter of interest (which is usually proportional to a phase) is encoded onto the state. There exists a plethora of state preparation techniques for creating highly quantum enhanced states, such as quantum state transfer from light to atoms [23–32], quantum non-demolition measurement (QND), [4, 18, 33–36], spin changing collisions [10, 11, 37–39], one-axis twisting (OAT) [3, 6, 8, 9, 40–42], two-axis counter-twisting (TACT) [40, 43], twist-and-turn squeezing (TNT) [16, 44], and adiabatically scanning through a quantum phase transition (QPT) [45–51]. However, the states generated via these schemes almost always require detection with very low noise (of the order of less than one particle) in order to see significant quantum enhancement [2, 52, 53].

Recently, there has been considerable interest in the concept of interaction-based readouts (IBRs) [50, 51, 54–66], which are periods of unitary evolution applied to the system *after* the phase encoding step, but *before* the measurement takes place. These readouts usually involve inter-particle interactions, similar to the ones used for the state preparation. Davis *et al.* showed that by using OAT to prepare a state with high quantum Fisher information (QFI), applying a phase shift, and then employing an IBR that reverses the OAT dynamics, quantum enhanced sensitivity could be achieved well beyond the Gaussian spin-squeezing regime. Furthermore, this quantum enhancement persisted even when the added detection noise was as large as the projection noise [54]. Similarly, Hosten *et al.* experimentally demonstrated that a period of nonlinear evolution after the state preparation and phase encoding could achieve sub SNL sensitivity in the presences of significant detection noise [55]. Macri *et al.* demonstrated that by performing an IBR that perfectly reverses the state preparation and then projects into the initial state, the sensitivity saturates the quantum Cramér-Rao bound (QCRB) [57]. Nolan *et al.* [60] further generalised this result to show that there exist *many* IBRs that satisfy the conditions for saturating the QCRB, and that the choice of IBR has implications for the level of sensitivity in the presence of detection noise (or "robustness"). In particular, it was found that the optimum IBR was not necessarily the one that perfectly reversed the state preparation. Furthermore, it was demonstrated that sensitivity approaching the Heisenberg limit [67, 68] could be achieved in the presence of detection noise approaching the number of particles. IBRs have also been explored by applying time-reversal of the state-preparation dynamics in systems where the quantum-enhanced state is generated via SCC [58, 59, 69], TACT [62], TNT [64], and QPT [50, 51].

In this work, we derive a limit for sensitivity in the presence of detection noise, which is significantly better than the levels achievable via previous schemes. We then present an IBR based on OAT that approaches this limit for states generated via OAT, TNT, TACT, QPT, and QND.

I. ULTIMATE SENSITIVITY LIMIT IN THE PRESENCE OF DETECTION NOISE

The sensitivity with which we can estimate the classical parameter ϕ is quantified via the Cramér-Rao bound: $\Delta\phi^2 = 1/F_C$, where F_C is the classical Fisher information (CFI), defined by $F_C = \sum_m \dot{P}_m^2/P_m$, where P_m is

* simon.a.haine@gmail.com

the probability of obtaining measurement result m, and $\dot{P}_m \equiv \partial_\phi P_m$. Assuming a collection of N particles distributed amongst two modes, the natural description for our system is provided via the *pseudo-spin* SU(2) algebra: $[\hat{J}_x, \hat{J}_y] = i\hat{J}_z$ [70]. The eigenstates of these operators form a natural basis of easily accessible measurements, as they can be obtained via single-particle operations such as linear rotations and particle counting [2]. For simplicity, throughout this paper we assume that measurements are made by projecting into the $\hat{J}_z$ basis, i.e. , $\{|m\rangle\langle m|\}$, where $\hat{J}_z|m\rangle = m|m\rangle$. The particular direction is of little consequence, however, as projections along other directions can be obtained via linear rotations. Following the convention introduced in [71] and subsequently used in [2, 50, 56, 60, 62, 64, 65, 69], we model the behaviour of an imperfect detector as sampling from the probability distribution

$$\tilde{P}_m(\sigma) = \sum_{m'} \Gamma_{m,m'}(\sigma) P_{m'}\,, \tag{1}$$

where

$$\Gamma_{m,m'}(\sigma) = e^{-(m-m')^2/(2\sigma^2)} / \sum_m e^{-(m-m')^2/(2\sigma^2)} \tag{2}$$

introduces detection noise of magnitude σ. This is equivalent to the positive operator valued measurement (POVM) $\{\hat{M}_m\} = \{\sum_{m'} \Gamma_{m,m'}|m'\rangle\langle m'|\}$. To demonstrate how the noise affects the CFI, we consider the case where P_m contains only two non-zero elements, P_a and P_b, with $P_b = 1 - P_a$, and $\dot{P}_a = -\dot{P}_b = \sqrt{F_0(P_a - P_a^2)}$, such that $F_C = F_0$. By approximating m as a continuous variable and extending the domain to $\pm\infty$ [72], we obtain

$$\tilde{P}(m) = (P_a e^{-(a-m)^2/2\sigma^2} + P_b e^{-(b-m)^2/2\sigma^2})/\sqrt{2\pi}\sigma\,. \tag{3}$$

Defining

$$\tilde{P}_a = \int_{-\infty}^{\frac{1}{2}(a+b)} \tilde{P}(m)dm \quad \text{and} \quad \tilde{P}_a = \int_{\frac{1}{2}(a+b)}^{\infty} \tilde{P}(m)dm \tag{4}$$

(assuming $a < b$), and maximising with respect to P_a ($P_a \to P_b \to \frac{1}{2}$) we obtain

$$F_C(\sigma) = \dot{\tilde{P}}_a^2/\tilde{P}_a + \dot{\tilde{P}}_b^2/\tilde{P}_b \approx F_0 \left(\text{Erf}\left[(a-b)/2\sqrt{2}\sigma\right]\right)^2. \tag{5}$$

Clearly, $F_C(\sigma)$ decays less rapidly when the separation between the non-zero components of P_m, $|a-b|$, is large compared to σ. This intuition leads us to postulate that distribution with maximum robustness, P_{opt} is

$$P_{N/2} = P_{-N/2} = \frac{1}{2}, \tag{6a}$$

$$\dot{P}_{N/2} = -\dot{P}_{-N/2} = \sqrt{F_0}/2, \tag{6b}$$

with all other elements equal to zero. While an analytic proof of this remains elusive, we confirm this via a numeric optimisation method [73]. In the absence of detection noise, the QCRB states that $F_C \leq F_Q$, where F_Q is the QFI. We define the *noisy QCRB* (NQCRB) as $F_C(\sigma) \leq F_n(\sigma)$, where $F_n(\sigma)$ is the CFI calculated from the $\{\tilde{P}_m(\sigma), \dot{\tilde{P}}_m(\sigma)\}$ obtained from performing the discrete sum in Eq. (1) numerically with $\{P_m, \dot{P}_m\} = \{P_{\text{opt}}, \dot{P}_{\text{opt}}\}$, and setting $F_0 = F_Q$. This is the maximum sensitivity that can be achieved by making spin measurements on a state with QFI equal to F_Q in the presence of detection noise σ. We can get an approximate analytic expression for $F_n(\sigma)$ by again approximating m as a continuous variable, but limiting the range to $-N/2 < m < N/2$, such that

$$F_n(\sigma) \approx F_Q \left(1 - 2\frac{\text{Erf}[\alpha/2]}{\text{Erf}[\alpha]}\right)^2, \tag{7}$$

with $\alpha = N/\sqrt{2}\sigma$. Fig.(1) shows excellent agreement between this expression and the exact value of $F_n(\sigma)$, calculated numerically. Eq. (7) provides a slight underestimate of the CFI, as information is lost when condensing P_m into a binary distribution via Eq. (4). For the remainder of this paper, we use the exact numeric value of $F_n(\sigma)$ rather than Eq. (7).

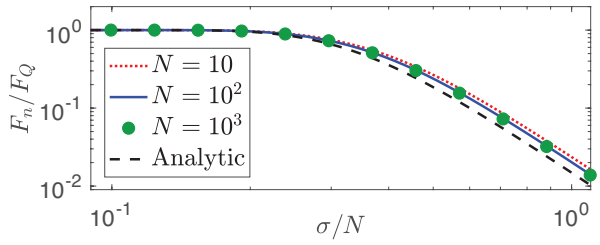


FIG. 1. The exact numeric value of F_n vs. σ/N for $N = 10$, 10^2 and 10^3, compared to the approximate expression Eq. (7). The shape of $F_n(\sigma/N)$ is almost identical for $N = 10^2$ and 10^3.

II. INTERACTION-BASED READOUT TO SATURATE THE NQCRB

The NQCRB sets the maximum achievable CFI in the presence of detection noise σ. What remains is to find an IBR that allows us to achieve this limit. Starting with an arbitrary initial pure state $|\psi_1\rangle$, we note that this state can always be written as $|\psi_1\rangle = U_1|\psi_0\rangle$, where $|\psi_0\rangle = |\frac{N}{2}\rangle$ is the maximal $\hat{J}_z$ eigenstate, which is completely separable in the particle basis. In most quantum enhanced metrology schemes, the unitary operator U_1 implements the *state preparation* step, which may be employed to increase the QFI of an initially separable state. Specific examples of this process including OAT, TACT, TNT, and QPT will be considered later. The phase shift ϕ is then encoded on to the state via $|\psi_\phi\rangle = e^{i\hat{J}_n\phi}|\psi_1\rangle$, where $\hat{J}_n = \mathbf{J}\cdot\mathbf{n}$, and $\mathbf{n}$ is a unit vector chosen to maximise

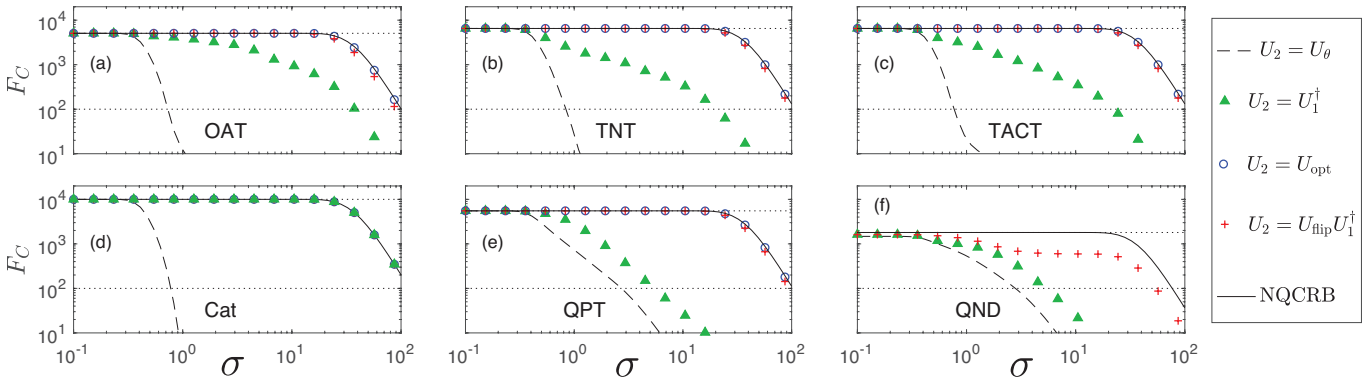


FIG. 2. $F_C(\sigma)$ for (a): OAT with $r = 0.2$, (b): TNT, (c): TACT, (d): OAT with $r = \frac{\pi}{2}$ (which corresponds to a spin-cat state), (e): QPT, and (f): QND. $U_\theta = e^{i\frac{\pi}{2}\hat{J}_y}$ for OAT, Cat, and TNT, and $U_\theta = 1$ for TACT, QPT, and QND. The upper and lower dotted black lines indicate the QCRB ($F_C = F_Q$) and SNL ($F_C = N$), respectively. $N = 100$ for all cases, and we have optimised over ϕ. The optimum ϕ is close to ϕ_0 for $U_2 = U_{\rm opt}$, and close to 0 for $U_2 = U_{\rm flip}U_1^\dagger$.

the QFI of $|\psi_\phi\rangle$. This vector can be obtained from the collective covariance matrix [20]. An IBR is some unitary U_2 such that measurements are made on the state $U_2|\psi_\phi\rangle$. Our goal is to find U_2 such that the probability distribution $P_m = |\langle m|U_2|\psi_\phi\rangle|^2$ saturates the NQCRB. It was shown in [57] that for $\phi \ll 1$, selecting $U_2 = U_1^\dagger$ saturates the QCRB. At some value $\phi = \phi_0$,

$$U_1^\dagger e^{i\hat{J}_n\phi_0}U_1|\psi_0\rangle = \frac{1}{\sqrt{2}}(|\psi_0\rangle + |\psi'\rangle) \equiv |\psi_b\rangle\,, \qquad (8)$$

where

$$|\psi'\rangle = (\hat{1} - |\psi_0\rangle\langle\psi_0|)|\psi_b\rangle/\sqrt{1 - |\langle\psi_b|\psi_0\rangle|^2}\,. \qquad (9)$$

We can artificially construct an IBR that is maximally robust to noise simply by constructing a unitary operator $U_{\rm p}$ that maps this state to one with distribution $P_{\rm opt}$:

$$U_{\rm p} = |\tfrac{N}{2}\rangle\langle\tfrac{N}{2}| + |\tfrac{-N}{2}\rangle\langle\psi'| + \sum_{m=-N/2+1}^{N/2-1} |m\rangle\langle m'|\,, \qquad (10)$$

where $\{|m'\rangle\}$ completes the orthogonal basis containing $|\frac{N}{2}\rangle$ and $|\psi'\rangle$. Thus, the optimum IBR is

$$U_2 = U_{\rm p}U_1^\dagger \equiv U_{\rm opt}. \qquad (11)$$

Fig. (2) shows the CFI calculated from $P_m = |\langle m|U_{\rm opt}|\psi_\phi\rangle|^2$ after convolving with detection noise, for quantum enhanced states generated from OAT, TACT, TNT, and QPT. Details of these states are provided in table (I) [74]. In all cases, we find that this IBR saturates the NQCRB. To understand the mechanism for this, we consider the effect of detection noise on the probability distributions. Fig. (3) shows $P_m(\phi)$ and $P_m(\phi+\delta\phi)$, with (right column) and without (left column) noise, for the case of OAT. When $U_2 = U_1^\dagger$ ((a) and (e)), the change in probability is centred around $m = \frac{N}{2}$ and nearby elements. When detection noise is added, $P_m(\phi)$ and $P_m(\phi+\delta\phi)$ become less distinct as the adjacent elements are mixed. However, by applying $U_2 = U_{\rm opt}$ ((b) and (f)), all of the probability in elements $m \neq \frac{N}{2}$ is transferred to $m = -\frac{N}{2}$ such that $P_m = P_{\rm opt}$. We stress that the application of $U_{\rm opt}$ does not effect the CFI in the absence of noise - the Hellinger distance

$$d_H^2 = 1 - \sum_m \sqrt{P_m(\phi)P_m(\phi+\delta\phi)} \qquad (12)$$

is identical in (a) and (b) ($d_H \approx 0.24$). However, $U_{\rm opt}$ *does* effect how distinguishable the states remain after the addition of detection noise: $d_H \approx 0.067$, and 0.201 for (e) and (f) respectively.

Scheme:	U_1	r
OAT	$e^{ir\hat{J}_z^2}e^{i\frac{\pi}{2}\hat{J}_y}$	0.2
TACT	$e^{ir(\hat{J}_x^2-\hat{J}_y^2)}$	0.032
TNT	$e^{ir(\hat{J}_z^2-\frac{N}{2}\hat{J}_x)}e^{i\frac{\pi}{2}\hat{J}_y}$	0.0715
Cat	$e^{ir\hat{J}_z^2}e^{i\frac{\pi}{2}\hat{J}_y}$	$\frac{\pi}{2}$
QPT	$\mathcal{T}\exp\left(\frac{-i}{\hbar}\int_0^{t_0}\hat{H}(t')dt'\right)e^{i\frac{\pi}{2}\hat{J}_y}$	

TABLE I. Details of the quantum state $|\psi_1\rangle = U_1|\frac{N}{2}\rangle$ used in Fig. (2). For TACT and TNT, r was chosen to maximise F_Q for $N = 100$, while for OAT, a moderate value of r was chosen such that the state was no longer in the spin-squeezed regime [54], but not sufficient to reach the maximum QFI spin-cat state, which occurs at $r = \frac{\pi}{2}$.

III. APPROACHING THE NQCRB WITH OAT-BASED IBRS

While our optimum IBR gives us insight into what maximises robustness, it is of no use to us unless we can find a physical mechanism with which it can be implemented. However, we can construct an IBR which has

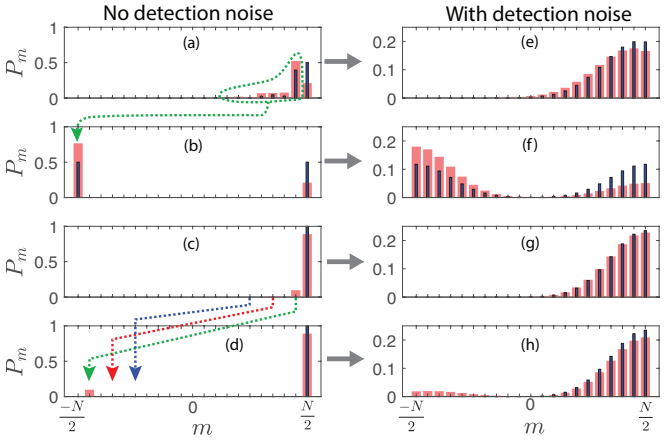


FIG. 3. $P_m(\phi)$ (blue thin bars) and $P_m(\phi+\delta\phi)$ (pink thick bars) with (right column) and without (left column) detection noise σ. (a) & (e): $U_2 = U_1^\dagger$, $\phi = \phi_0$. (b)&(f): $U_2 = U_{\rm opt}$, $\phi = \phi_0$. (c)&(g): $U_2 = U_1^\dagger$, $\phi = 0$. (d)&(h) $U_2 = U_{\rm flip}U_1^\dagger$, $\phi = 0$. The Hellinger distance d_H is (a-d): 0.238, (e): 0.067, (f): 0.201, (g): 0.012, (h): 0.232. Parameters: $N = 20$, $\sigma = 3$, $r = 0.2$, $\delta_\phi = \frac{1}{N}$, $\phi_0 = 0.118$. The behaviour of $U_{\rm p}$ and $U_{\rm flip}$ is indicated by the arrows between (a)&(b), and (c)&(d), respectively.

similar properties to the ideal case with the OAT mechanism. The OAT unitary can be used to create the well known spin-cat state [75, 76]:

$$e^{i\frac{\pi}{2}\hat{J}_y^2}|m\rangle = \tfrac{1}{\sqrt{2}}e^{i\frac{\pi}{4}}(|m\rangle + i(-1)^m|-m\rangle) \equiv |\beta(m)\rangle\,, \quad (13)$$

for even N [77]. This state has the unusual property that $|\langle\beta(m)|e^{i\frac{\pi}{2}\hat{J}_z}|\beta(m)\rangle|^2 = \cos^2\frac{m\pi}{2}$. That is, even-$m$ states are unaffected by a π rotation, while odd-m states become orthogonal. As such, a $\frac{\pi}{2}$ phase shift followed by secondary application of $e^{i\frac{\pi}{2}\hat{J}_y^2}$ will return $|\beta(m)\rangle$ to $|m\rangle$ if m is even, or transfer it to an orthogonal state if m is odd. Specifically

$$e^{i\frac{\pi}{2}\hat{J}_y^2}e^{i\frac{\pi}{2}\hat{J}_z}e^{i\frac{\pi}{2}\hat{J}_y^2} = -\sum_m i^{m(m-1)}|-1^m m\rangle\langle m| \equiv U_{\rm flip}\,. \quad (14)$$

The action of $U_{\rm flip}$ is to exchange the odd elements of P_m with P_{-m}, while leaving the even elements unaffected, as illustrated in fig.(3) (d) and (h) [78]. For sufficiently small ϕ, most of the CFI for the state $U_1^\dagger|\psi_\phi\rangle$ is usually contained in the elements $m = \frac{N}{2}$ and $m = \frac{N}{2}-1$ ((c) and (g)). Applying $U_{\rm flip}$ to this state transfers probability from $m = \frac{N}{2}-1$ to $m = -(\frac{N}{2}-1)$, forming a distribution *almost* as robust as $P_{\rm opt}$.

Fig. (2) shows the performance of this scheme compared to $U_{\rm opt}$ for quantum enhanced states generated via OAT, TACT, and TNT (see table (I)). In these three cases we see that $U_2 = U_{\rm flip}U_1^\dagger$ is very close to the optimum case ($U_2 = U_{\rm opt}$ and the NQCRB), and achieves sensitivity very close to the QCRB for detection noise σ significantly exceeding $\sqrt{N}$. For comparison, we have also included the previously considered case of an *echo*, where $U_2 = U_1^\dagger$, which performs significantly better than the case of no IBR ($U_2 = U_\theta$, where only a linear rotation is used to maximise the CFI), but not nearly as well as $U_2 = U_{\rm flip}U_1^\dagger$. We have also included the special case of OAT with $r = \frac{\pi}{2}$, which corresponds to the maximum QFI spin-cat state. In this case, both $U_2 = U_{\rm flip}U_1^\dagger$ and $U_2 = U_1^\dagger$ saturate the NQCRB, while the case of no IBR loses all quantum enhancement for $\sigma \lessapprox 1$. The reason why there is no need for the extra application of $U_{\rm flip}$ is because the state $U_1^\dagger|\psi_\phi\rangle$ already yields a probability distribution identical to $P_{\rm opt}$, and is unchanged by application of $U_{\rm flip}$. The outstanding performance of the echo IBR for this state was first reported in [60] and subsequently in [61, 65], but it was not known that this is the maximum achievable sensitivity [79].

We also considered QPT, where the increased QFI is generated by slowly varying the parameters in a time-dependent Hamiltonian, such that the ground state is adiabatically transformed to one with high QFI. We implemented this with a Hamiltonian of the form

$$\hat{H} = \hbar\chi(\hat{J}_x\cos^2\tfrac{\pi}{2}\tfrac{t}{t_0} + \hat{J}_z^2\sin^2\tfrac{\pi}{2}\tfrac{t}{t_0}), \quad (15)$$

such that

$$U_1 = \mathcal{T}\left[\exp\left(\tfrac{-i}{\hbar}\int_0^{t_0}\hat{H}(t')dt'\right)\right]e^{i\frac{\pi}{2}\hat{J}_y}, \quad (16)$$

where $\mathcal{T}$ represents the time-ordering operator. In the limit $\chi t_0 \to \infty$, $U_1|\frac{N}{2}\rangle = |0\rangle$, the twin-Fock state. We chose a moderate value $\chi t_0 = 20$, such that the final state contains non-zero elements on either side of $m = 0$. Unlike the previous examples, when making measurements on the state $U_1^\dagger|\psi_\phi\rangle$ for small ϕ, most of the CFI is contained in the elements $m = \frac{N}{2}$ and $m = \frac{N}{2}-2$, such that $U_{\rm flip}$ has little effect. This is easily rectified, however, by using a modified IBR with $U'_{\rm flip} = e^{i\frac{\pi}{2}\hat{J}_y^2}e^{i\frac{\pi}{4}\hat{J}_z}e^{i\frac{\pi}{2}\hat{J}_y^2}$, which for $N \gg 1$, $U_{\rm flip}|m\rangle \approx |-m\rangle$ if $m/2$ is odd. We see in Fig. (2e) that this IBR is very close to the NQCRB.

The benefit of our IBR is not limited to pure states. We consider a quantum enhanced mixed state

$$\rho = \sum_m e^{-\frac{m^2}{\Delta^2}}|m\rangle\langle m|/(\sum_m e^{-\frac{m^2}{\Delta^2}}). \quad (17)$$

We chose $\Delta = 1$, which corresponds to a state with significant quantum enhancement, yet is far from pure, with the purity $\gamma = {\rm Tr}[\rho^2] \approx 0.4$. Such a state may arise from quantum enhancement via a strong QND interaction with a detuned optical field, as described in [80], with an imperfect measurement leading to uncertainty in m. Unlike the previous states considered, this state is mixed, so there is no unitary operator that maps this distribution to $P_{\rm opt}$. However, at $\phi = 0$, the final distribution is similar to the QPT case, which inspires us to use the same IBR, namely $U_2 = U_{\rm flip}U_1^\dagger$, with U_1 generated via

the adiabatic evolution considered in the QPT example. We see in Fig. (2f) that while this case isn't as robust as previous examples, the general trend is the same, that is $U_2 = U_{\text{flip}}U_1^\dagger$ is more robust than $U_2 = U_1^\dagger$, which in turn outperforms $U_2 = U_\theta$. As the state is mixed, we cannot systematically construct U_{opt}. For completeness, we have also investigated applying our IBR to states with no quantum enhancement, such as coherent spin-states [81], and find qualitatively similar results [82].

IV. DISCUSSION

The results of this paper may form an integral part of future quantum-enhanced sensing technologies, as high-QFI states are particularly susceptible to detection noise. While OAT-based quantum enhancement schemes are not yet capable of manufacturing spin-cat states (and therefore U_{flip}), progress in this area is rapid, particularly in schemes based on optically induced non-linearities [6, 18], and Rydberg atoms [83]. Furthermore, we have provided insight and a systematic approach for constructing a robust IBR. Armed with this insight, schemes that approximate our optimum scheme may be found through other dynamical mechanisms that are perhaps easier to implement in a particular system. For example, it has been shown that QPT can be used to engineer spin-cat states [46], so could potentially be used to construct a near-optimum IBR. One might question the wisdom of using an IBR that requires the ability to create a maximum QFI cat state in cases where the QFI of the input state is less than this. However, there may be situations when it is impractical to use a state preparation capable of creating a cat state, such as when the preparation time is limited [63]. Similarly, a state with less quantum enhancement may be desirable in the presence of external phase noise. In these situations, the presence of unavoidably large detection noise will still necessitate the use of a high-performance IBR in order to achieve high sensitivity. Finally, the NQCRB provides a limit for the performance of all IBR's. Once the sensitivity approaches this limit, further gains can only be made through the reduction of detection noise, rather than via improvement of the IBR.

ACKNOWLEDGMENTS

The author acknowledges fruitful discussions with Samuel Nolan, Safoura Mirkhalaf, Luca Pezze, Augusto Smerzi, Manuel Gessner, and Jacob Dunningham. This work was supported by the European Union's Horizon 2020 research and innovation programme under the Marie Sklodowska-Curie grant agreement No. 704672.

[1] Alexander D. Cronin, Jörg Schmiedmayer, and David E. Pritchard, "Optics and interferometry with atoms and molecules," Rev. Mod. Phys. **81**, 1051–1129 (2009).
[2] L. Pezze, A. Smerzi, M. K. Oberthaler, R. Schmied, and P. Treutlein, "Quantum metrology with nonclassical states of atomic ensembles," arXiv:1609.01609 (2016).
[3] J. Esteve, C. Gross, Weller. A., S. Giovanazzi, and M. K. Oberthaler, "Squeezing and entanglement in a Bose-Einstein condensate," Nature **455**, 1216 (2008).
[4] J. Appel, P. J. Windpassinger, D. Oblak, U. B. Hoff, N. Kjaergaard, and E. S. Polzik, "Mesoscopic atomic entanglement for precision measurements beyond the standard quantum limit," Proceedings of the National Academy of Sciences **106**, 10960–10965 (2009).
[5] Ian D. Leroux, Monika H. Schleier-Smith, and Vladan Vuletić, "Implementation of cavity squeezing of a collective atomic spin," Phys. Rev. Lett. **104**, 073602 (2010).
[6] Monika H. Schleier-Smith, Ian D. Leroux, and Vladan Vuletić, "Squeezing the collective spin of a dilute atomic ensemble by cavity feedback," Phys. Rev. A **81**, 021804 (2010).
[7] Monika H. Schleier-Smith, Ian D. Leroux, and Vladan Vuletić, "States of an ensemble of two-level atoms with reduced quantum uncertainty," Phys. Rev. Lett. **104**, 073604 (2010).
[8] C. Gross, T. Zibold, E. Nicklas, J. Estève, and M. K. Oberthaler, "Nonlinear atom interferometer surpasses classical precision limit," Nature **464**, 1165–1169 (2010).
[9] Max F. Riedel, Pascal Böhi, Yun Li, Theodor W. Hänsch, Alice Sinatra, and Philipp Treutlein, "Atom-chip-based generation of entanglement for quantum metrology," Nature **464**, 1170–1173 (2010).
[10] B. Lücke, M. Scherer, J. Kruse, L. Pezze, F. Deuretzbacher, P. Hyllus, O. Topic, J. Peise, W. Ertmer, J. Arlt, L. Santos, A. Smerzi, and C. Klempt, "Twin matter waves for interferometry beyond the classical limit," Science **334**, 773–776 (2011).
[11] C. D. Hamley, C. S. Gerving, T. M. Hoang, E. M. Bookjans, and M. S. Chapman, "Spin-nematic squeezed vacuum in a quantum gas," Nat Phys **8**, 305–308 (2012).
[12] T. Berrada, S. van Frank, R. Bücker, T. Schumm, J. F. Schaff, and J Schmiedmayer, "Integrated Mach–Zehnder interferometer for Bose–Einstein condensates," Nature Communications **4**, 2077 EP – (2013).
[13] Caspar F. Ockeloen, Roman Schmied, Max F. Riedel, and Philipp Treutlein, "Quantum metrology with a scanning probe atom interferometer," Phys. Rev. Lett. **111**, 143001 (2013).
[14] Helmut Strobel, Wolfgang Muessel, Daniel Linnemann, Tilman Zibold, David B. Hume, Luca Pezzè, Augusto Smerzi, and Markus K. Oberthaler, "Fisher information and entanglement of non-gaussian spin states," Science **345**, 424–427 (2014).
[15] W. Muessel, H. Strobel, D. Linnemann, D. B. Hume, and M. K. Oberthaler, "Scalable spin squeezing for quantum-enhanced magnetometry with bose-einstein condensates," Phys. Rev. Lett. **113**, 103004 (2014).
[16] W. Muessel, H. Strobel, D. Linnemann, T. Zibold, B. Julia-Diaz, and M. K. Oberthaler, "Twist-and-turn spin squeezing in Bose-Einstein condensates,"

arXiv:1507.02930 (2015).
[17] I. Kruse, K. Lange, J. Peise, B. Lücke, L. Pezzè, J. Arlt, W. Ertmer, C. Lisdat, L. Santos, A. Smerzi, and C. Klempt, "Improvement of an atomic clock using squeezed vacuum," Phys. Rev. Lett. **117**, 143004 (2016).
[18] Onur Hosten, Nils J. Engelsen, Rajiv Krishnakumar, and Mark A. Kasevich, "Measurement noise 100 times lower than the quantum-projection limit using entangled atoms," Nature **529**, 505 EP – (2016).
[19] Yi-Quan Zou, Ling-Na Wu, Qi Liu, Luo, Xin-Yu Lu, Shuai-Feng Guo Guo, Jia-Hao Cao, Tey, and Li Meng Khoon, You, "Beating the classical precision limit with spin-1 Dicke state of more than 10000 atoms," arXiv:1802.10288 (2018).
[20] Philipp Hyllus, Otfried Gühne, and Augusto Smerzi, "Not all pure entangled states are useful for sub-shot-noise interferometry," Phys. Rev. A **82**, 012337 (2010).
[21] Philipp Hyllus, Wiesław Laskowski, Roland Krischek, Christian Schwemmer, Witlef Wieczorek, Harald Weinfurter, Luca Pezzé, and Augusto Smerzi, "Fisher information and multiparticle entanglement," Phys. Rev. A **85**, 022321 (2012).
[22] Géza Tóth, "Multipartite entanglement and high-precision metrology," Phys. Rev. A **85**, 022322 (2012).
[23] G. S. Agarwal and R. R. Puri, "Cooperative behavior of atoms irradiated by broadband squeezed light," Phys. Rev. A **41**, 3782–3791 (1990).
[24] A. Kuzmich, Klaus Mølmer, and E. Polzik, "Spin squeezing in an ensemble of atoms illuminated with squeezed light," Phys. Rev. Lett. **79**, 4782–4785 (1997).
[25] M. G. Moore, O. Zobay, and P. Meystre, "Quantum optics of a Bose-Einstein condensate coupled to a quantized light field," Phys. Rev. A **60**, 1491–1506 (1999).
[26] Hui Jing, Jing-Ling Chen, and Mo-Lin Ge, "Quantum-dynamical theory for squeezing the output of a Bose-Einstein condensate," Phys. Rev. A **63**, 015601 (2000).
[27] Michael Fleischhauer and Shangqing Gong, "Stationary source of nonclassical or entangled atoms," Phys. Rev. Lett. **88**, 070404 (2002).
[28] S. A. Haine and J. J. Hope, "Outcoupling from a Bose-Einstein condensate with squeezed light to produce entangled-atom laser beams," Phys. Rev. A **72**, 033601 (2005).
[29] S. A. Haine and J. J. Hope, "A multi-mode model of a non-classical atom laser produced by outcoupling from a Bose-Einstein condensate with squeezed light," Laser Physics Letters **2**, 597–602 (2005).
[30] S. A. Haine, M. K. Olsen, and J. J. Hope, "Generating controllable atom-light entanglement with a Raman atom laser system," Phys. Rev. Lett. **96**, 133601 (2006).
[31] Stuart S. Szigeti, Behnam Tonekaboni, Wing Yung S. Lau, Samantha N. Hood, and Simon A. Haine, "Squeezed-light-enhanced atom interferometry below the standard quantum limit," Phys. Rev. A **90**, 063630 (2014).
[32] Simon A. Haine, Stuart S. Szigeti, Matthias D. Lang, and Carlton M. Caves, "Heisenberg-limited metrology with information recycling," Phys. Rev. A **91**, 041802 (2015).
[33] Kuzmich, A., Bigelow, N. P., and Mandel, L., "Atomic quantum non-demolition measurements and squeezing," Europhys. Lett. **42**, 481–486 (1998).
[34] A. Kuzmich, L. Mandel, and N. P. Bigelow, "Generation of spin squeezing via continuous quantum nondemolition measurement," Phys. Rev. Lett. **85**, 1594–1597 (2000).
[35] Anne Louchet-Chauvet, Jürgen Appel, Jelmer J Renema, Daniel Oblak, Niels Kjaergaard, and Eugene S Polzik, "Entanglement-assisted atomic clock beyond the projection noise limit," New Journal of Physics **12**, 065032 (2010).
[36] Klemens Hammerer, Anders S. Sørensen, and Eugene S. Polzik, "Quantum interface between light and atomic ensembles," Rev. Mod. Phys. **82**, 1041–1093 (2010).
[37] L.-M. Duan, A. Sørensen, J. I. Cirac, and P. Zoller, "Squeezing and entanglement of atomic beams," Phys. Rev. Lett. **85**, 3991–3994 (2000).
[38] H. Pu and P. Meystre, "Creating macroscopic atomic Einstein-Podolsky-Rosen states from Bose-Einstein condensates," Phys. Rev. Lett. **85**, 3987–3990 (2000).
[39] Samuel P. Nolan, Jacopo Sabbatini, Michael W. J. Bromley, Matthew J. Davis, and Simon A. Haine, "Quantum enhanced measurement of rotations with a spin-1 Bose-Einstein condensate in a ring trap," Phys. Rev. A **93**, 023616 (2016).
[40] Masahiro Kitagawa and Masahito Ueda, "Squeezed spin states," Phys. Rev. A **47**, 5138–5143 (1993).
[41] Anders S. Sørensen and Klaus Mølmer, "Entanglement and extreme spin squeezing," Phys. Rev. Lett. **86**, 4431–4434 (2001).
[42] S. A. Haine, J. Lau, R. P. Anderson, and M. T. Johnsson, "Self-induced spatial dynamics to enhance spin squeezing via one-axis twisting in a two-component Bose-Einstein condensate," Phys. Rev. A **90**, 023613 (2014).
[43] Jian Ma and Xiaoguang Wang, "Fisher information and spin squeezing in the Lipkin-Meshkov-Glick model," Phys. Rev. A **80**, 012318 (2009).
[44] C. K. Law, H. T. Ng, and P. T. Leung, "Coherent control of spin squeezing," Phys. Rev. A **63**, 055601 (2001).
[45] Chaohong Lee, "Adiabatic mach-zehnder interferometry on a quantized Bose-Josephson junction," Phys. Rev. Lett. **97**, 150402 (2006).
[46] Chaohong Lee, "Universality and anomalous mean-field breakdown of symmetry-breaking transitions in a coupled two-component Bose-Einstein condensate," Phys. Rev. Lett. **102**, 070401 (2009).
[47] Z. Zhang and L.-M. Duan, "Generation of massive entanglement through an adiabatic quantum phase transition in a spinor condensate," Phys. Rev. Lett. **111**, 180401 (2013).
[48] Haijun Xing, Anbang Wang, Qing-Shou Tan, Wenxian Zhang, and Su Yi, "Heisenberg-scaled magnetometer with dipolar spin-1 condensates," Phys. Rev. A **93**, 043615 (2016).
[49] Xin-Yu Luo, Yi-Quan Zou, Ling-Na Wu, Qi Liu, Ming-Fei Han, Meng Khoon Tey, and Li You, "Deterministic entanglement generation from driving through quantum phase transitions," Science **355**, 620–623 (2017).
[50] P. Feldmann, M. Gessner, M. Gabbrielli, C. Klempt, L. Santos, L. Pezzè, and A. Smerzi, "Interferometric sensitivity and entanglement by scanning through quantum phase transitions in spinor Bose-Einstein condensates," Phys. Rev. A **97**, 032339 (2018).
[51] Jiahao Huang, Min Zhuang, and Chaohong Lee, "Non-Gaussian precision metrology via driving through quantum phase transitions," Phys. Rev. A **97**, 032116 (2018).
[52] Rafal Demkowicz-Dobrzanski, Jan Kolodynski, and Madalin Guta, "The elusive Heisenberg limit in quantum-enhanced metrology," Nat Commun **3**, 1063

(2012).
[53] R. Demkowicz-Dobrzanski, M. Jarzyna, and J. Kolodynski, "Quantum limits in optical interferometry," Progress in Optics **345** (2015).
[54] E. Davis, G. Bentsen, and M. Schleier-Smith, "Approaching the Heisenberg limit without single-particle detection," Phys. Rev. Lett. **116**, 053601 (2016).
[55] O. Hosten, R. Krishnakumar, N. J. Engelsen, and M. A. Kasevich, "Quantum phase magnification," Science **352**, 1552–1555 (2016).
[56] Florian Fröwis, Pavel Sekatski, and Wolfgang Dür, "Detecting large quantum Fisher information with finite measurement precision," Phys. Rev. Lett. **116**, 090801 (2016).
[57] Tommaso Macrì, Augusto Smerzi, and Luca Pezzè, "Loschmidt echo for quantum metrology," Phys. Rev. A **94**, 010102 (2016).
[58] D. Linnemann, H. Strobel, W. Muessel, J. Schulz, R. J. Lewis-Swan, K. V. Kheruntsyan, and M. K. Oberthaler, "Quantum-enhanced sensing based on time reversal of nonlinear dynamics," Phys. Rev. Lett. **117**, 013001 (2016).
[59] Stuart S. Szigeti, Robert J. Lewis-Swan, and Simon A. Haine, "Pumped-up SU(1,1) interferometry," Phys. Rev. Lett. **118**, 150401 (2017).
[60] Samuel P. Nolan, Stuart S. Szigeti, and Simon A. Haine, "Optimal and robust quantum metrology using interaction-based readouts," Phys. Rev. Lett. **119**, 193601 (2017).
[61] Renpang Fang, Resham Sarkar, and Selim Shahriar, "Enhancing sensitivity of an atom interferometer to the Heisenberg limit using increased quantum noise," arXiv:1707.08260 (2018).
[62] Fabian Anders, Luca Pezzè, Augusto Smerzi, and Carsten Klempt, "Phase magnification by two-axis countertwisting for detection-noise robust interferometry," Phys. Rev. A **97**, 043813 (2018).
[63] Anthony J Hayes, Shane Dooley, William J Munro, Kae Nemoto, and Jacob Dunningham, "Making the most of time in quantum metrology: concurrent state preparation and sensing," Quantum Science and Technology **3**, 035007 (2018).
[64] Safoura S. Mirkhalaf, Samuel P. Nolan, and Simon A. Haine, "Robustifying twist-and-turn entanglement with interaction-based readout," Phys. Rev. A **97**, 053618 (2018).
[65] Jiahao Huang, Min Zhuang, Bo Lu, Yongguan Ke, and Chaohong Lee, "Achieving heisenberg-limited metrology with spin cat states via interaction-based readout," Phys. Rev. A **98**, 012129 (2018).
[66] R. J. Lewis-Swan, M. A. Norcia, J. R. K. Cline, J. K. Thompson, and A. M. Rey, "Robust spin squeezing via photon-mediated interactions on an optical clock transition," arXiv:1804.06784 (2018).
[67] M. J. Holland and K. Burnett, "Interferometric detection of optical phase shifts at the Heisenberg limit," Phys. Rev. Lett. **71**, 1355–1358 (1993).
[68] Vittorio Giovannetti, Seth Lloyd, and Lorenzo Maccone, "Quantum metrology," Phys. Rev. Lett. **96**, 010401 (2006).
[69] Marco Gabbrielli, Luca Pezzè, and Augusto Smerzi, "Spin-mixing interferometry with Bose-Einstein condensates," Phys. Rev. Lett. **115**, 163002 (2015).
[70] Bernard Yurke, Samuel L. McCall, and John R. Klauder, "SU(2) and SU(1,1) interferometers," Phys. Rev. A **33**, 4033–4054 (1986).
[71] Luca Pezzé and Augusto Smerzi, "Ultra sensitive two-mode interferometry with single-mode number squeezing," Phys. Rev. Lett. **110**, 163604 (2013).
[72] See the supplemental material for further details of the derivation of Eq. (7).
[73] See the supplemental material for further details of the optimisation method.
[74] For further details on these quantum states, see the supplemental material. By 'quantum-enhanced states', we mean 'states with $F_Q > N$'.
[75] G. S. Agarwal, R. R. Puri, and R. P. Singh, "Atomic Schrödinger cat states," Phys. Rev. A **56**, 2249–2254 (1997).
[76] Samuel P. Nolan and Simon A. Haine, "Quantum Fisher information as a predictor of decoherence in the preparation of spin-cat states for quantum metrology," Phys. Rev. A **95**, 043642 (2017).
[77] For odd N we require an additional rotation: an equal superposition cat is generated by $e^{i\frac{\pi}{2}\hat{J}_y}e^{i\frac{\pi}{2}\hat{J}_y^2}|m\rangle$.
[78] For odd N, an IBR that performs the same function is given by $U_{\text{flip}} = e^{i\frac{\pi}{2}\hat{J}_y(\hat{J}_y+1)}e^{i\theta\hat{J}_z}e^{i\frac{\pi}{2}\hat{J}_y(\hat{J}_y+1)}$, with $\theta = \frac{\pi}{2}(1+1/N)$.
[79] We note that [61] reports higher robustness than this. However, the state is identical, and the discrepancy is due to a different convention for the detection noise.
[80] Simon A. Haine and Stuart S. Szigeti, "Quantum metrology with mixed states: When recovering lost information is better than never losing it," Phys. Rev. A **92**, 032317 (2015).
[81] J. M. Radcliffe, "Some properties of coherent spin states," Journal of Physics A: General Physics **4**, 313 (1971).
[82] The plot of $F_C(\sigma)$ for the coherent spin state is provided in the supplementary material.
[83] Hannes Busche, Paul Huillery, Simon W. Ball, Teodora Ilieva, Matthew P. A. Jones, and Charles S. Adams, "Contactless nonlinear optics mediated by long-range Rydberg interactions," Nature Physics **13**, 655 EP – (2017).

SUPPLEMENTAL MATERIAL

In this supplemental material I provide further details about the derivation of the noisy quantum Cramér-Rao bound (NQCRB), and provide further details about the quantum states used in this manuscript.

V. DERIVATION OF EQ. (5)

Beginning with Eq. (1),

$$\tilde{P}_m = \sum_{m'} \Gamma_{m,m'}(\sigma) P_{m'} \,, \tag{18}$$

and Eq. (2),

$$\Gamma_{m,m'}(\sigma) = \frac{e^{-(m-m')^2/(2\sigma^2)}}{\sum_m e^{-(m-m')^2/(2\sigma^2)}} \,, \tag{19}$$

we can obtain an approximate expression for the case when P_m contains only two non-zero elements, at $m = a$ and $m = b$. By treating the discrete probability distribution as continuous, we obtain

$$P(m) = P_a \delta(m-a) + P_b \delta(m-b) \,. \tag{20}$$

Replacing the discrete sum in Eq. (18) with a continuous integral, we find

$$\tilde{P}(m) = \int_{-\infty}^{\infty} \Gamma(m-m') P(m') dm \tag{21}$$

where

$$\Gamma(m-m') = \frac{1}{\sigma\sqrt{2\pi}} e^{-(m-m')^2/(2\sigma^2)} \,. \tag{22}$$

Defining

$$\tilde{P}_a = \int_{-\infty}^{\frac{1}{2}(a+b)} \tilde{P}(m) dm \tag{23a}$$

$$\tilde{P}_b = \int_{\frac{1}{2}(a+b)}^{\infty} \tilde{P}(m) dm \tag{23b}$$

gives

$$\tilde{P}_a = \tfrac{1}{2}\left(1 + (2P_a - 1)\mathrm{Erf}\left[\frac{b-a}{2\sqrt{2}\sigma}\right]\right) \tag{24a}$$

$$\tilde{P}_b = \tfrac{1}{2}\left(1 + (1 - 2P_a)\mathrm{Erf}\left[\frac{b-a}{2\sqrt{2}\sigma}\right]\right) \tag{24b}$$

where we have used $P_b = 1 - P_a$. Similarly, we find

$$\dot{\tilde{P}}_a = \dot{P}_a \mathrm{Erf}\left[\frac{b-a}{2\sqrt{2}\sigma}\right] \tag{25a}$$

$$\dot{\tilde{P}}_b = -\dot{P}_a \mathrm{Erf}\left[\frac{b-a}{2\sqrt{2}\sigma}\right] \tag{25b}$$

where we have used $\dot{P}_b = -\dot{P}_a$. Using these equations in $F_C(\sigma) = \dot{\tilde{P}}_a^2/\tilde{P}_a + \dot{\tilde{P}}_b^2/\tilde{P}_b$ gives

$$F_C(\sigma) = \frac{4\dot{P}_a^2 \mathrm{Erf}\left[\frac{b-a}{2\sqrt{2}\sigma}\right]^2}{(1-2P_a)^2 \mathrm{Erf}\left[\frac{b-a}{2\sqrt{2}\sigma}\right]^2 - 1} \tag{26}$$

Setting $\dot{P}_a = \sqrt{F_0(P_a - P_a^2)}$, such that

$$F_C(\sigma = 0) = \frac{\dot{P}_a^2}{P_a} + \frac{\dot{P}_b^2}{P_b} = F_0\,, \tag{27}$$

gives

$$F_C(\sigma) = F_0 \frac{4P_a(1-P_a)\mathrm{Erf}\left[\frac{b-a}{2\sqrt{2}\sigma}\right]^2}{1-(1-2P_a)^2\mathrm{Erf}\left[\frac{b-a}{2\sqrt{2}\sigma}\right]^2}\,. \tag{28}$$

Maximising this function with respect to P_a (Setting $\partial_{P_a} F_C(\sigma) = 0$ and solving for P_a) gives $P_a = \frac{1}{2}$, and therefore

$$F_C(\sigma) = F_0 \mathrm{Erf}\left[\frac{b-a}{2\sqrt{2}\sigma}\right]^2\,. \tag{29}$$

VI. OPTIMUM PROBABILITY DISTRIBUTION IN THE PRESENCE OF DETECTION NOISE

In this section we demonstrate that of all probability distributions with $F_C = F_0$, P_{opt}, the distribution with $P_{\frac{N}{2}} = P_{-\frac{N}{2}} = \frac{1}{2}$, $\dot{P}_{\frac{N}{2}} = -\dot{P}_{-\frac{N}{2}} = \sqrt{F_0}/2$, displays the maximum sensitivity in the presence of detection noise σ. We introduce the vectors

$$\mathbf{v} = \left[\sqrt{P_{-\frac{N}{2}}}, \sqrt{P_{-\frac{N}{2}+1}}, \ldots, \sqrt{P_{\frac{N}{2}-1}}, \sqrt{P_{\frac{N}{2}}}\right]^T \tag{30a}$$

$$\begin{aligned}\dot{\mathbf{v}} &= \partial_\phi \left[\sqrt{P_{-\frac{N}{2}}}, \sqrt{P_{-\frac{N}{2}+1}}, \ldots, \sqrt{P_{\frac{N}{2}-1}}, \sqrt{P_{\frac{N}{2}}}\right]^T \\ &= \frac{1}{2}\left[\frac{\dot{P}_{-\frac{N}{2}}}{\sqrt{P_{-\frac{N}{2}}}}, \frac{\dot{P}_{-\frac{N}{2}+1}}{\sqrt{P_{-\frac{N}{2}+1}}}, \ldots, \frac{\dot{P}_{\frac{N}{2}-1}}{\sqrt{P_{\frac{N}{2}-1}}}, \frac{\dot{P}_{\frac{N}{2}}}{\sqrt{P_{\frac{N}{2}}}}\right]^T\,,\end{aligned} \tag{30b}$$

such that

$$F_C = 4\dot{\mathbf{v}}^T\dot{\mathbf{v}} = \sum_m \frac{\dot{P}_m^2}{P_m}\,. \tag{31}$$

Using this notation, its straightforward to transform our distribution such that $\mathbf{v}' = A\mathbf{v}$, $\dot{\mathbf{v}}' = A\dot{\mathbf{v}}$, where A is a square orthogonal real matrix with the property $A^TA = AA^T = 1$. Importantly, such a transformation preserves the CFI:

$$\begin{aligned}F_C(\mathbf{v}') &= 4(\dot{\mathbf{v}}')^T\dot{\mathbf{v}}' \\ &= 4\left(A\dot{\mathbf{v}}\right)^T\left(A\dot{\mathbf{v}}\right) \\ &= 4\dot{\mathbf{v}}^TA^TA\dot{\mathbf{v}} \\ &= 4\dot{\mathbf{v}}^T\dot{\mathbf{v}} = F_C(\mathbf{v})\,.\end{aligned} \tag{32}$$

To confirm that P_{opt} is in fact the distribution with maximum robustness, we begin with an arbitrary probability distribution P_{arb} that satisfies $F_C\left[P_{\mathrm{arb}}, \dot{P}_{\mathrm{arb}}\right] = F_0$, and then employ a numeric optimisation algorithm, which is implemented as follows:

1. Calculate $\{\mathbf{v}, \dot{\mathbf{v}}\}$ from $\{P_m, \dot{P}_m\}$.

2. Rotate $\mathbf{v}$ and $\dot{\mathbf{v}}$ by a small angle of randomly generated magnitude about a randomly generated axis in $N+1$ dimensional space. This process is represented by an orthogonal real matrix A, and therefore conserves $F_C(\sigma = 0)$.

3. Calculate $\{P_m, \dot{P}_m\}$ from the new $\{\mathbf{v}, \dot{\mathbf{v}}\}$.

4. Add detection noise to this new distribution via Eq. (18) and Eq. (19), and calculate $F_C(\sigma)$. If the $F_C(\sigma)$ has increased, we accept this new distribution, and repeat. Otherwise, we keep the original distribution, and repeat.

Fig. 4 (a-c) shows the CFI after addition of detection noise for 10^5 iterations of this algorithm, for three different initial distributions, all with $\dot{P}_m$ chosen such that $F_C(0) = 1$. However, each distribution has a different CFI in the presence of noise. The CFI (with detection noise) rapidly converges to the CFI of P_{opt}. The evolution of the Hellinger distance between these distributions and P_{opt} approaches zero (d-f). We repeated this process for several different values of σ and initial distributions, and in all cases found convergence to P_{opt}.

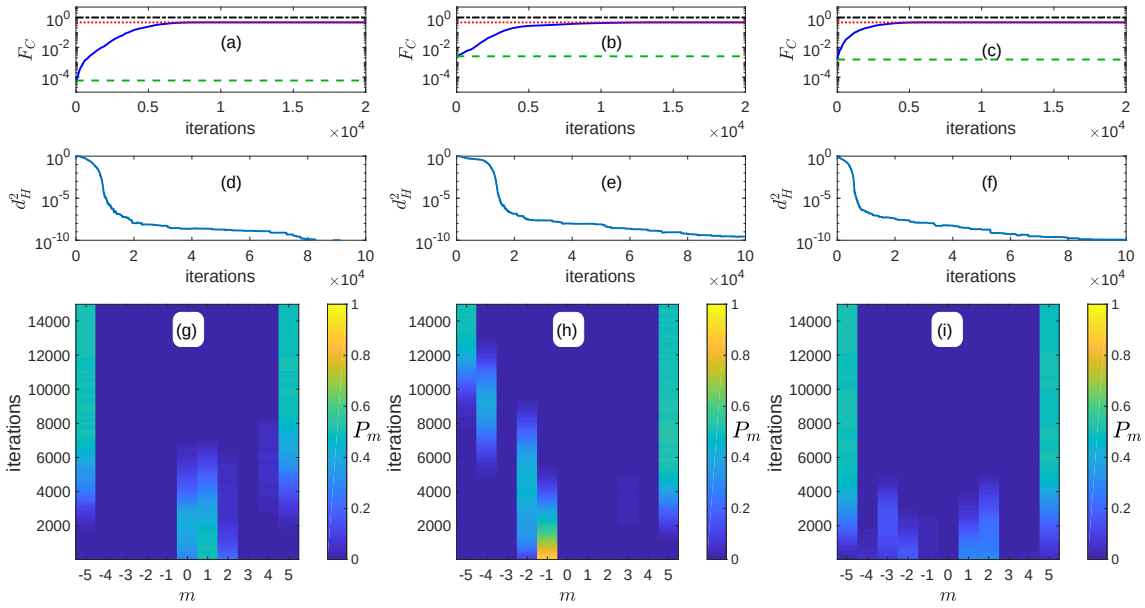


FIG. 4. (a-c): The CFI in the presence of detection noise σ, $F_C(\sigma)$ as a function of the number of iterations of the optimisation algorithm (blue line), compared to the initial value (green dashed line). We have also show $F_C(\sigma)$ for P_{opt}, which is the NQCRB (red dotted line). The CFI without noise ($F_C(0)$) remains constant for all iterations, and is identical to the $F_C(0)$ for P_{opt} (black dot dashed line). (d-f): The Hellinger distance between P and P_{opt} vs. the number of iterations. (g-i): The evolution of the probability distributions corresponding to the above frames. Parameters: $N = 10$, $\sigma = 4$.

To ensure that our optimisation algorithm is not getting 'stuck' in a local maximum, we generate entirely random distributions satisfying the constraint that $F_C\left[P, \dot{P}\right] = F_0$, by employing a randomly generated transformation matrix to P_{opt}. We see in Fig. (5) that while $F_C(0)$ remains constant, $F_C(\sigma)$ does not exceed the optimum value, calculated from P_{opt}. Again, we employed different initial distributions and values of σ.

VII. DERIVATION OF EQUATION 6

As before, we approximate P_{opt} as a continuous distribution such that

$$P(m) = \tfrac{1}{2}\left(\delta(m + \tfrac{N}{2}) + \delta(m - \tfrac{N}{2})\right) \tag{33}$$

$$\dot{P}(m) = \frac{\sqrt{F_0}}{2}\left(\delta(m + \tfrac{N}{2}) - \delta(m - \tfrac{N}{2})\right). \tag{34}$$

To derive equation (5) we made the approximation that the domain of integration extended to infinity, which is reasonable as long as $|a|, |b| \ll N/2$. However, in order to get a more accurate approximation, we now restrict our domain to $\{-N/2, N/2\}$. Approximating $\Gamma_{m,m'}$ as a continuous function, and enforcing the correct normalisation

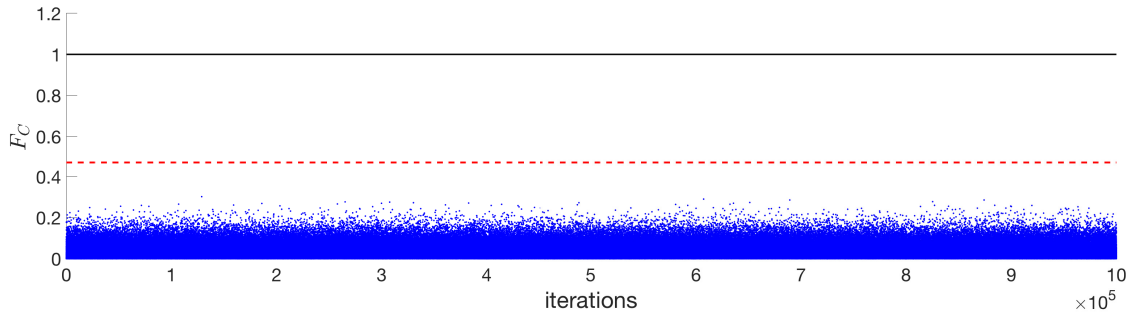


FIG. 5. Blue dots: $F_C(\sigma)$ for randomly generated distributions with $F_C(0) = 1$. $F_C(\sigma)$ does not exceed the NQCRB, indicated by the red dashed line. Parameters: $N = 10$, $\sigma = 4$.

conditions gives

$$\begin{aligned}\tilde{P}(m) &= \int_{-N/2}^{N/2} P(m')\Gamma(m-m')dm' \\ &= \frac{1}{\sigma \mathrm{Erf}\left[\frac{N}{\sqrt{2}\sigma}\right]}\left(\exp\left(\frac{\left(m-\frac{N}{2}\right)^2}{2\sigma^2}\right)+\exp\left(\frac{\left(m+\frac{N}{2}\right)^2}{2\sigma^2}\right)\right) \qquad (35)\\ \dot{\tilde{P}}(m) &= \int_{-N/2}^{N/2} P(m')\Gamma(m-m')dm' \\ &= \frac{\sqrt{F_0}}{\sigma \mathrm{Erf}\left[\frac{N}{\sqrt{2}\sigma}\right]}\left(\exp\left(\frac{\left(m-\frac{N}{2}\right)^2}{2\sigma^2}\right)-\exp\left(\frac{\left(m+\frac{N}{2}\right)^2}{2\sigma^2}\right)\right). \qquad (36)\end{aligned}$$

Defining $\tilde{P}_a$ and $\tilde{P}_b$ as before, we find

$$\tilde{P}_a = \int_{-N/2}^{0} \tilde{P}(m)dm = \frac{1}{2} \qquad (37a)$$

$$\tilde{P}_b = \int_{0}^{N/2} \tilde{P}(m)dm = \frac{1}{2} \qquad (37b)$$

$$(37c)$$

and

$$\dot{\tilde{P}}_a = \int_{-N/2}^{0} \dot{\tilde{P}}(m)dm = \sqrt{F_0}\left(\frac{1}{2} - \frac{\mathrm{Erf}\left[N/2\sqrt{2}\sigma\right]}{\mathrm{Erf}\left[N/\sqrt{2}\sigma\right]}\right) \qquad (38a)$$

$$\dot{\tilde{P}}_b = \int_{0}^{N/2} \dot{\tilde{P}}(m)dm = \sqrt{F_0}\left(-\frac{1}{2} + \frac{\mathrm{Erf}\left[N/2\sqrt{2}\sigma\right]}{\mathrm{Erf}\left[N/\sqrt{2}\sigma\right]}\right). \qquad (38b)$$

Using these equations in $F_C(\sigma) = \dot{\tilde{P}}_a^2/P_a + \dot{\tilde{P}}_b^2/P_b$ gives

$$F_C(\sigma) = F_0\left(1 - 2\frac{\mathrm{Erf}[N/2\sqrt{2}\sigma]}{\mathrm{Erf}[N/\sqrt{2}\sigma]}\right)^2. \qquad (39)$$

If we choose our IBRO such that the measurement saturates the QCRB in the absence of noise, we replace F_0 with F_Q, and arrive at equation (6) of the main text.

VIII. FURTHER DETAILS OF THE QUANTUM STATES USED IN FIGURE 2

In this section we give further details about the states used in figure (2) of the main text. We have used the Husimi Q-function as a visualisation tool, defined by

$$Q(\theta,\phi) = \frac{N+1}{4\pi}\langle\theta,\phi|\rho|\theta,\phi\rangle \tag{40}$$

with $\rho = |\psi_1\rangle\langle\psi_1|$, and

$$|\theta,\phi\rangle = \exp(i\phi\hat{J}_z)\exp(i\theta\hat{J}_y)|\frac{N}{2}\rangle\,. \tag{41}$$

Additionally, $N = 100$ was used throughout.

A. OAT

The OAT state is generated via $|\psi_1\rangle = U_1|\frac{N}{2}\rangle$, where

$$U_1 = \exp\left(ir\hat{J}_z^2\right)\exp\left(i\tfrac{\pi}{2}\hat{J}_y\right). \tag{42}$$

For figure (2), we chose $r = 0.2$. Fig. 6 shows the QFI, probability distribution, and Husimi Q-Function.

B. TNT

The TNT state is generated via $|\psi_1\rangle = U_1|\frac{N}{2}\rangle$, where

$$U_1 = \exp\left(ir\left(\hat{J}_z^2 - \frac{N}{2}\hat{J}_x\right)\right)\exp(i\tfrac{\pi}{2}\hat{J}_y). \tag{43}$$

For figure (2), we chose $r = 0.0715$, which is the value at which the QFI is maximum. The Husimi Q-function, probability distribution, and QFI for this state are shown in Fig. 7.

C. TACT

The TACT state is generated via $|\psi_1\rangle = U_1|\frac{N}{2}\rangle$, where

$$U_1 = \exp\left(ir\left(\hat{J}_x^2 - \hat{J}_y^2\right)\right). \tag{44}$$

For figure (2), we chose $r = 0.032$, which is the value at which the QFI is maximum. The Husimi Q-function, probability distribution, and QFI for this state are shown in Fig. 8.

D. Cat

The cat state is generated via $|\psi_1\rangle = U_1|\frac{N}{2}\rangle$, where

$$\exp\left(ir\hat{J}_z^2\right)\exp\left(i\tfrac{\pi}{2}\hat{J}_y\right). \tag{45}$$

with $r = \pi/2$, which is the value at which the QFI is maximum. The Husimi Q-function, probability distribution, and QFI for this state are shown in Fig. 9.

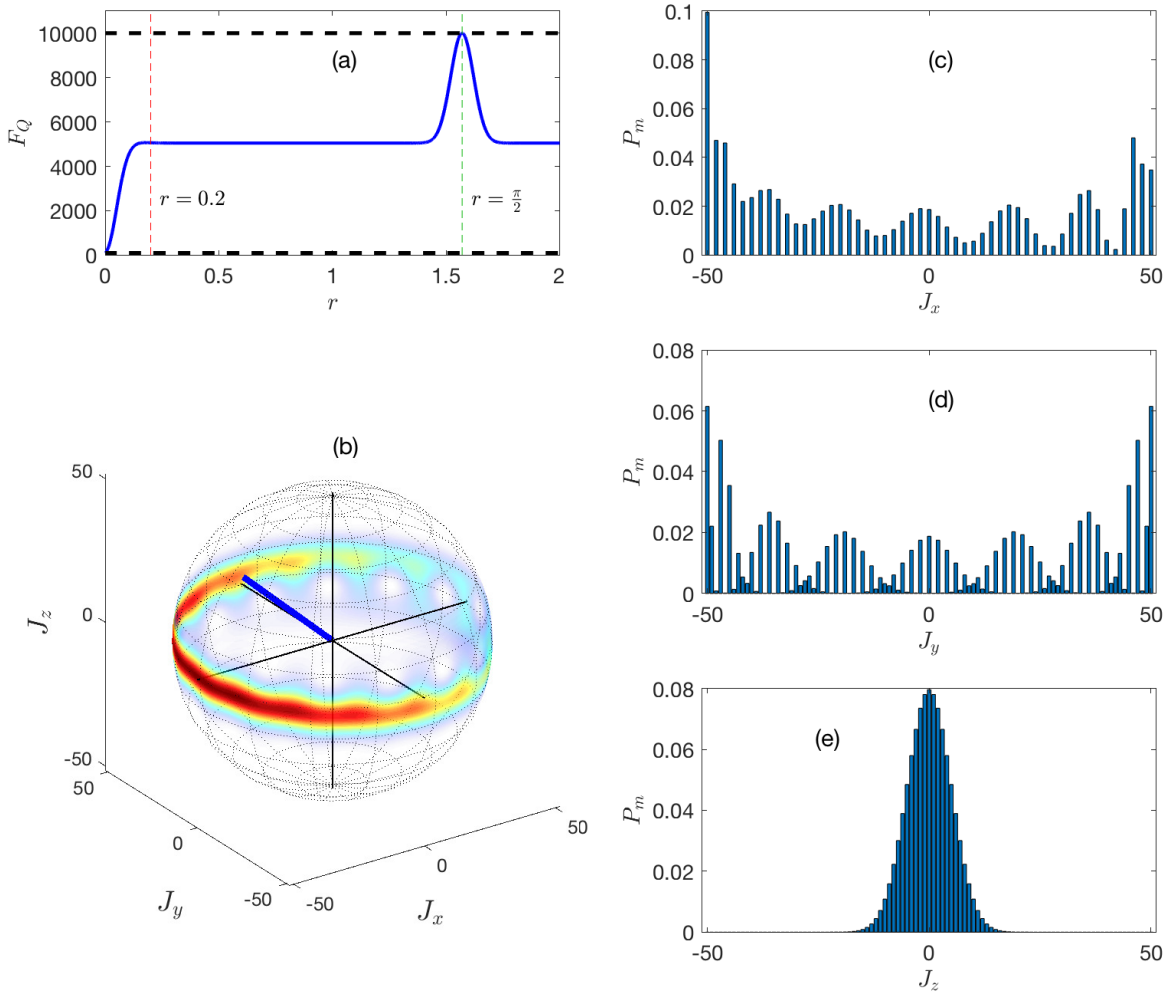


FIG. 6. Properties of the OAT state: $|\psi_1\rangle = \exp(ir\hat{J}_z^2)\exp(i\frac{\pi}{2}\hat{J}_y)|\frac{N}{2}\rangle$. (a): The QFI is calculated via $F_Q = 4\left(\langle\psi_1|\hat{J}_n^2|\psi_1\rangle - |\langle\psi_1|\hat{J}_n|\psi_1\rangle|^2\right)$, where $\hat{J}_n$ is the pseudo-spin operator along which the QFI is maximum. The value of r used in figure (2) ($r = 0.2$) is indicated by the vertical red line. The lower and upper dashed black lines indicate the shot-noise limit ($F_Q = N$) and Heisenberg limit ($F_Q = N^2$), respectively. (b) $Q(\theta, \phi)$. The direction of $\hat{J}_n$ is indicated by the thick blue line. (c-e): The probability distribution $P_m = |\langle m_j|\psi_1\rangle|^2$, where m_j is the mth eigenstate of $\hat{J}_j$, for $j = \{x, y, z\}$.

E. QPT

The QPT state was generated via evolution by a time-dependent Hamiltonian of the form

$$\hat{H} = \hbar\chi(\hat{J}_x \cos^2\tfrac{\pi}{2}\tfrac{t}{t_0} + \hat{J}_z^2 \sin^2\tfrac{\pi}{2}\tfrac{t}{t_0}), \tag{46}$$

such that

$$U_1 = \left(\mathcal{T}\exp\left(\tfrac{-i}{\hbar}\int_0^{t_0}\hat{H}(t')dt'\right)\right)\exp(i\frac{\pi}{2}\hat{J}_y), \tag{47}$$

where $\mathcal{T}$ represents the time-ordering operator. In the limit $\chi t_0 \to \infty$, $U_1|\frac{N}{2}\rangle = |0\rangle$, the twin-Fock state. We chose a moderate value $\chi t_0 = 20$, such that the final state contains non-zero elements on either side of $m = 0$. The Husimi Q-function, probability distribution, and QFI for this state are shown in Fig. (10).

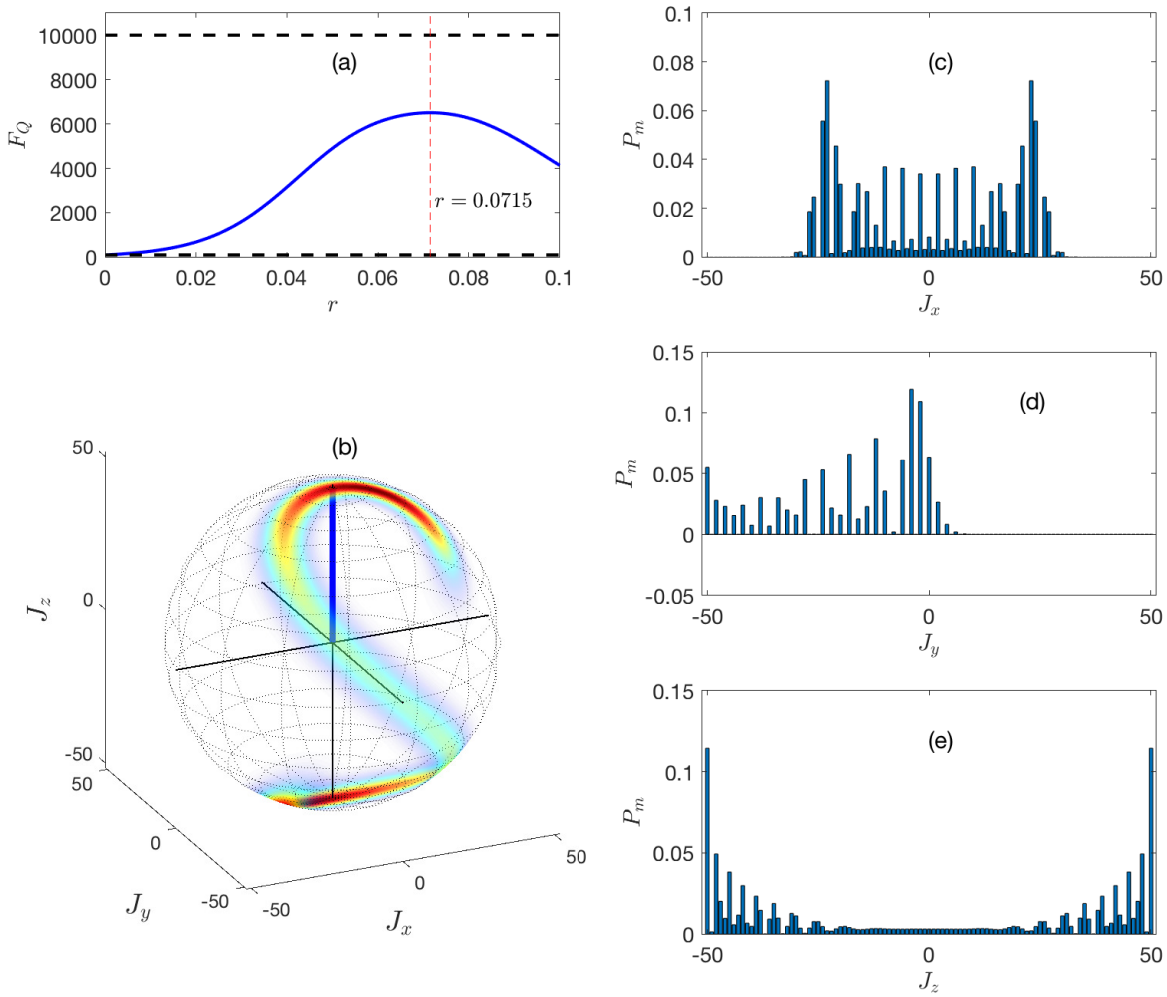


FIG. 7. Properties of the TNT state: $|\psi_1\rangle = \exp\left(ir\left(\hat{J}_z^2 - \frac{N}{2}\hat{J}_x\right)\right)\exp(i\frac{\pi}{2}\hat{J}_y)|\frac{N}{2}\rangle$. (a): The QFI is calculated via $F_Q = 4\left(\langle\psi_1|\hat{J}_n^2|\psi_1\rangle - |\langle\psi_1|\hat{J}_n|\psi_1\rangle|^2\right)$, where $\hat{J}_n$ is the pseudo-spin operator along which the QFI is maximum. The value of r used in figure (2) ($r = 0.0715$) is indicated by the vertical red line. The lower and upper dashed black lines indicate the shot-noise limit ($F_Q = N$) and Heisenberg limit ($F_Q = N^2$), respectively. (b) $Q(\theta, \phi)$. The direction of $\hat{J}_n$ is indicated by the thick blue line. (c-e): The probability distribution $P_m = |\langle m_j|\psi_1\rangle|^2$, where m_j is the mth eigenstate of $\hat{J}_j$, for $j = \{x, y, z\}$.

F. QND

The QND state is was selected as a mixture of $\hat{J}_z$ eigenstates. Specifically

$$\rho = \frac{\sum_m \exp\left(-\frac{m^2}{\Delta^2}\right)|m\rangle\langle m|}{\left(\sum_m e^{-\frac{m^2}{\Delta^2}}\right)}. \tag{48}$$

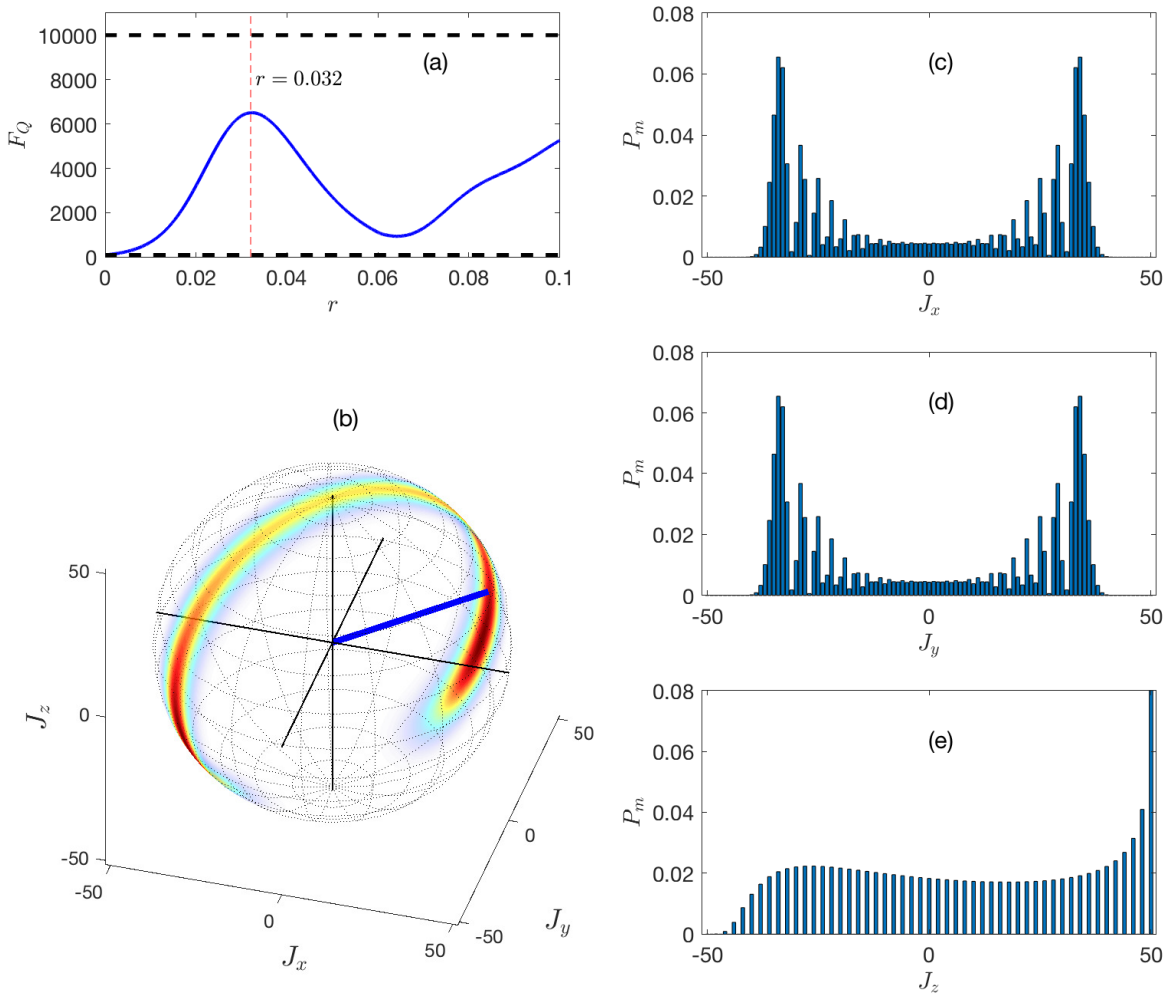


FIG. 8. Properties of the TACT state: $|\psi_1\rangle = \exp\left(ir\left(\hat{J}_x^2 - \hat{J}_y^2\right)\right)|\frac{N}{2}\rangle$. (a): The QFI is calculated via $F_Q = 4\left(\langle\psi_1|\hat{J}_n^2|\psi_1\rangle - |\langle\psi_1|\hat{J}_n|\psi_1\rangle|^2\right)$, where $\hat{J}_n$ is the pseudo-spin operator along which the QFI is maximum. The value of r used in figure (2) ($r = 0.032$) is indicated by the vertical red line. The lower and upper dashed black lines indicate the shot-noise limit ($F_Q = N$) and Heisenberg limit ($F_Q = N^2$), respectively. (b) $Q(\theta, \phi)$. The direction of $\hat{J}_n$ is indicated by the thick blue line. (c-e): The probability distribution $P_m = |\langle m_j|\psi_1\rangle|^2$, where m_j is the mth eigenstate of $\hat{J}_j$, for $j = \{x, y, z\}$.

In order to calculate the QFI of a mixed state, we must use $F_Q = \mathrm{Tr}[\rho(\hat{L}[\rho])^2]$, where $\hat{L}$ is the symmetric logarithmic derivative. For our case, the QFI takes the from

$$F_Q = \sum_{i,j} \frac{2|\langle e_i|\hat{J}_n|e_j\rangle|^2(\lambda_i - \lambda_j)^2}{\lambda_i + \lambda_j} \tag{49}$$

where $\rho|e_j\rangle = \lambda_j|e_j\rangle$. For our state, $\hat{J}_n$ lies in the $x - y$ plane, so for definitiveness we chose $\hat{J}_n = \hat{J}_y$. The Husimi Q-function, probability distribution, and QFI for this state are shown in Fig. 11.

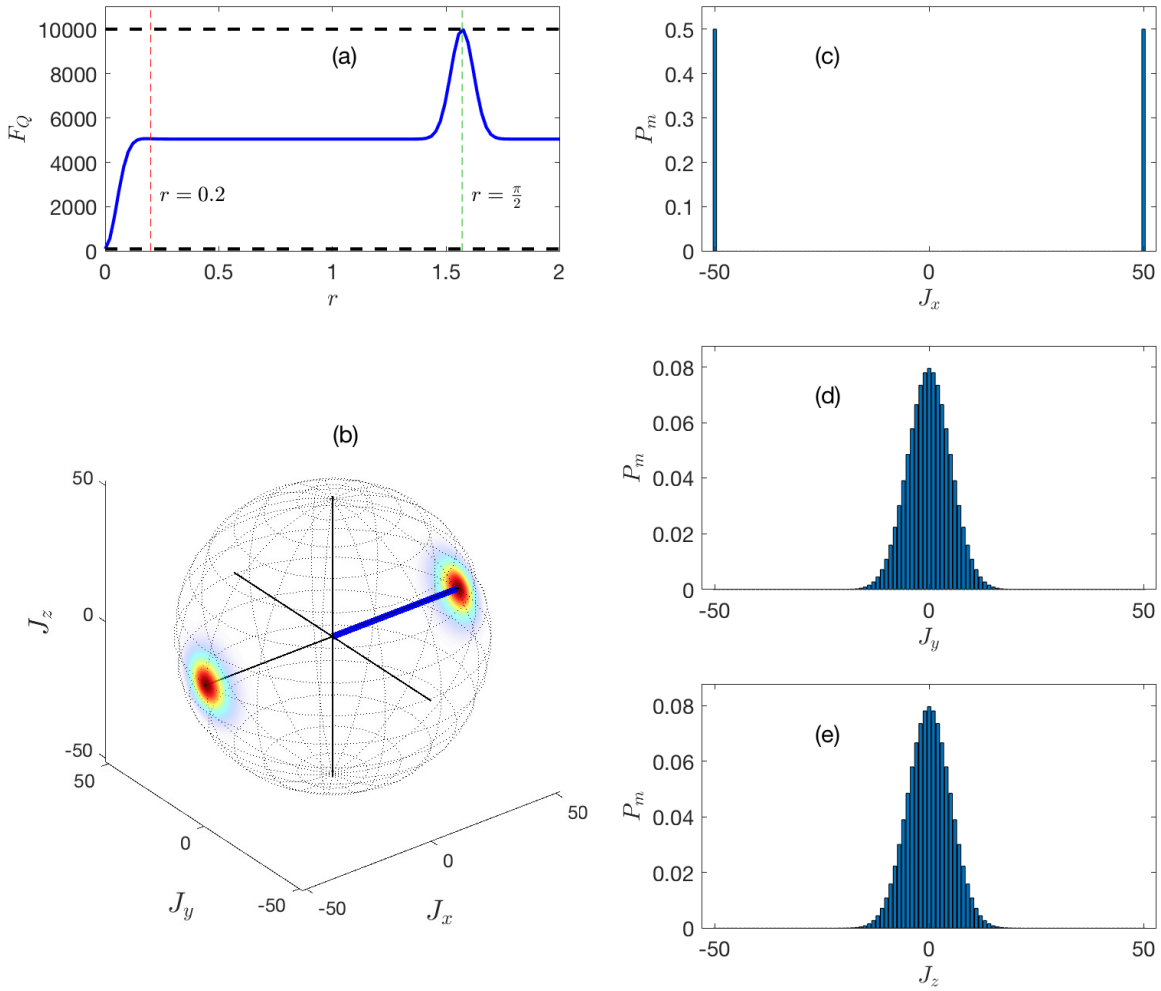


FIG. 9. Properties of the cat state: $|\psi_1\rangle = \exp\left(ir\hat{J}_z^2\right)\exp\left(i\frac{\pi}{2}\hat{J}_y\right)|\frac{N}{2}\rangle$, for $r = \pi/2$. (a): The QFI is calculated via $F_Q = 4\left(\langle\psi_1|\hat{J}_n^2|\psi_1\rangle - |\langle\psi_1|\hat{J}_n|\psi_1\rangle|^2\right)$, where $\hat{J}_n$ is the pseudo-spin operator along which the QFI is maximum. The lower and upper dashed black lines indicate the shot-noise limit ($F_Q = N$) and Heisenberg limit ($F_Q = N^2$), respectively. (b) $Q(\theta, \phi)$. The direction of $\hat{J}_n$ is indicated by the thick blue line. (c-e): The probability distribution $P_m = |\langle m_j|\psi_1\rangle|^2$, where m_j is the mth eigenstate of $\hat{J}_j$, for $j = \{x, y, z\}$.

G. Coherent Spin State

For completeness, we consider the coherent spin state given by $|\psi_1\rangle = U_1|\frac{N}{2}\rangle$, where

$$U_1 = \exp\left(i\frac{\pi}{2}\hat{J}_y\right). \tag{50}$$

Fig. (12) shows $F_C(\sigma)$ for the different IBRO. We see the same general trend as throughout the rest of the paper, except that $U_2 = U_\theta$ and $U_2 = U_1$ are identical.

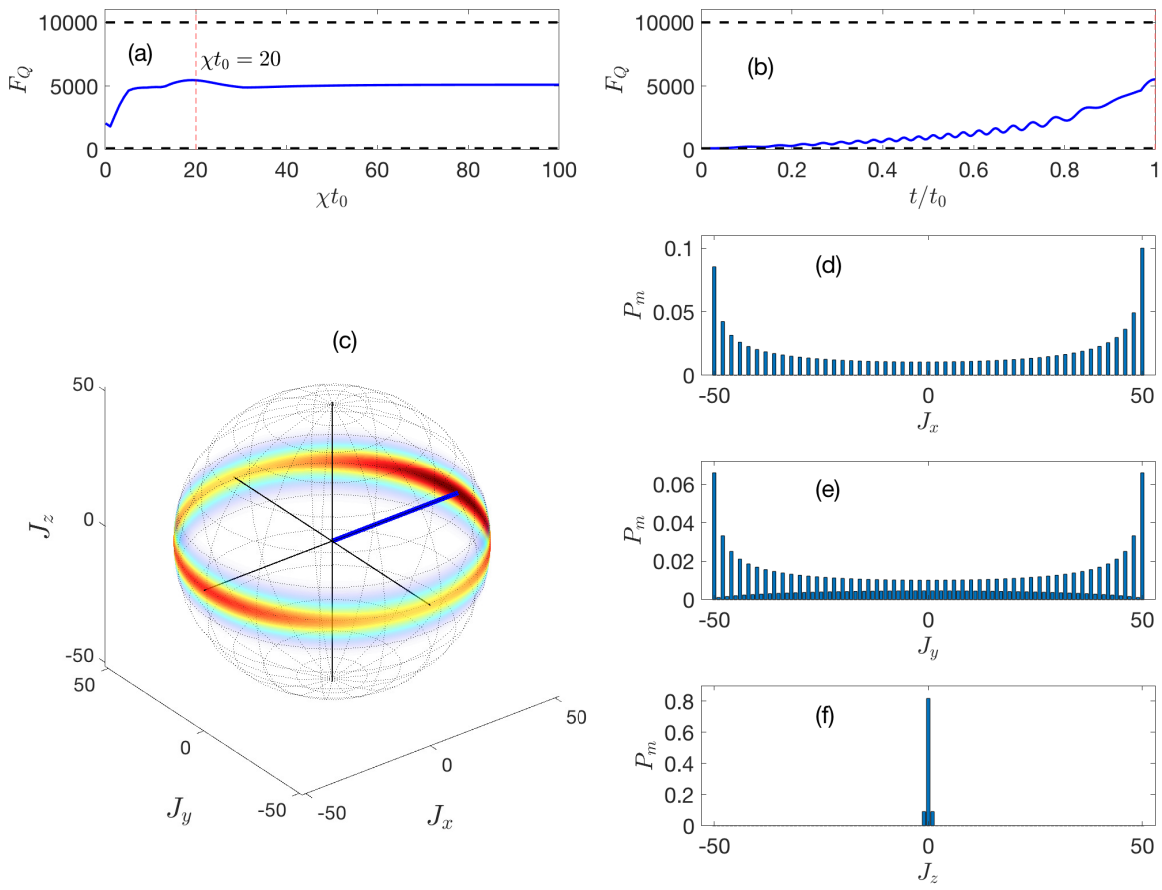


FIG. 10. Properties of the QPT state: $|\psi_1\rangle = U_1 = (\mathcal{T}\exp(\frac{-i}{\hbar}\int_0^{t_0}\hat{H}(t')dt'))\exp(i\frac{\pi}{2}\hat{J}_y)|\frac{N}{2}\rangle$, where $\hat{H} = \hbar\chi(\hat{J}_x\cos^2\frac{\pi}{2}\frac{t}{t_0} + \hat{J}_z^2\sin^2\frac{\pi}{2}\frac{t}{t_0})$. (a): The QFI is calculated via $F_Q = 4\left(\langle\psi_1|\hat{J}_n^2|\psi_1\rangle - |\langle\psi_1|\hat{J}_n|\psi_1\rangle|^2\right)$, where $\hat{J}_n$ is the pseudo-spin operator along which the QFI is maximum, as a function of χt_0, where t_0 is the maximum time. (b): The QFI as a function of t/t_0, for $\chi t_0 = 20$. In (a) and (b), the lower and upper dashed black lines indicate the shot-noise limit ($F_Q = N$) and Heisenberg limit ($F_Q = N^2$), respectively. (c) $Q(\theta,\phi)$. The direction of $\hat{J}_n$ is indicated by the thick blue line. (d-f): The probability distribution $P_m = |\langle m_j|\psi_1\rangle|^2$, where m_j is the mth eigenstate of $\hat{J}_j$, for $j = \{x, y, z\}$.

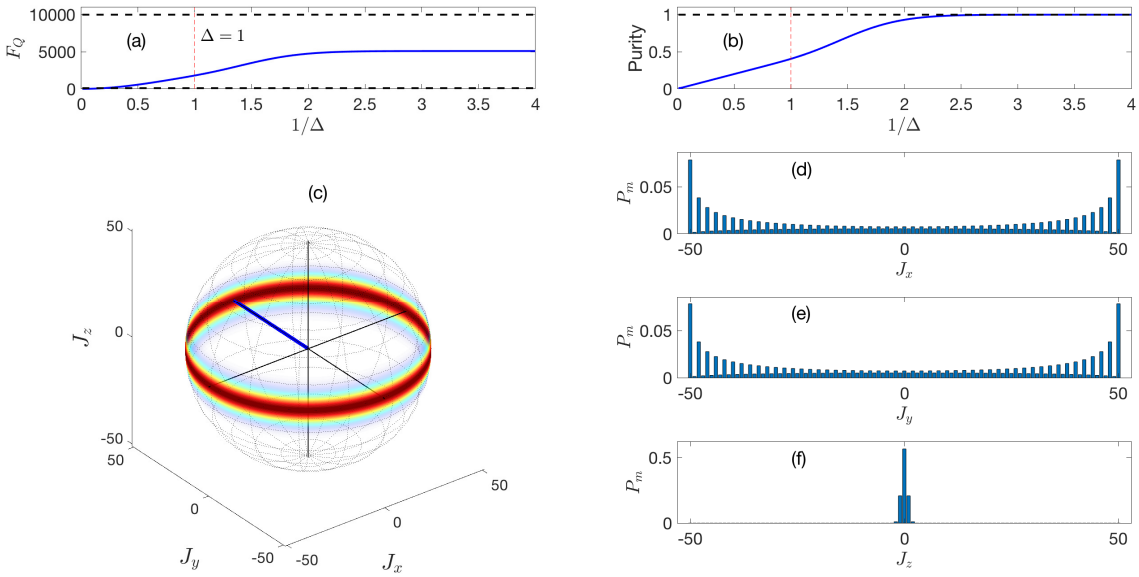


FIG. 11. Properties of the QND state: $\rho = \sum_m e^{-\frac{m^2}{\Delta^2}} |m\rangle\langle m| / (\sum_m e^{-\frac{m^2}{\Delta^2}})$, for $\Delta = 1$. (a): The QFI is calculated via Eq. (49). The lower and upper dashed black lines indicate the shot-noise limit ($F_Q = N$) and Heisenberg limit ($F_Q = N^2$), respectively. (b): The purity $\gamma = \mathrm{Tr}[\rho^2]$. (c) $Q(\theta, \phi)$. For our state, $\hat{J}_n$ lies in the $x - y$ plane, so for definitiveness we chose $\hat{J}_n = \hat{J}_y$ (indicated by the thick blue line). (d-f): The probability distribution $P_m = |\langle m_j | \psi_1 \rangle|^2$, where m_j is the mth eigenstate of $\hat{J}_j$, for $j = \{x, y, z\}$.

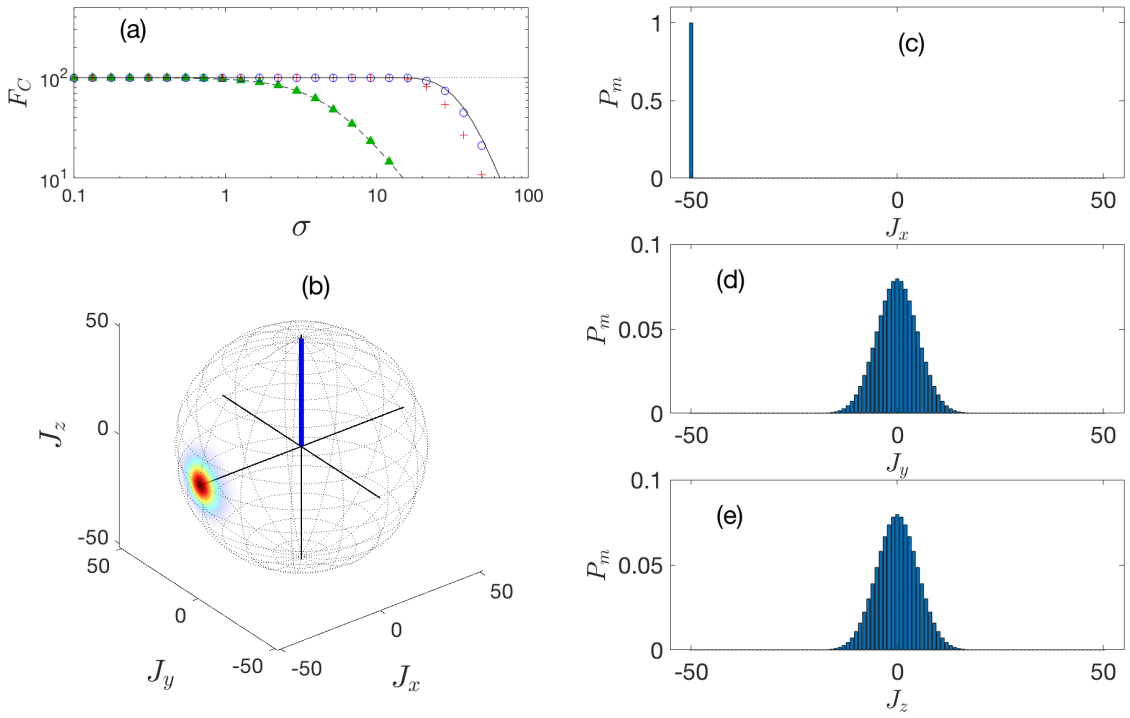


FIG. 12. Properties of the CSS state: $|\psi_1\rangle = \exp\left(i\frac{\pi}{2}\hat{J}_y\right)|\frac{N}{2}\rangle$. (a): $F_C(\sigma)$ for $U_2 = U_\theta$ (dashed line), $U_2 = U_1$ (green triangles), $U_2 = U_{\text{flip}}U_1$, (red plus symbols), $U_2 = U_{\text{opt}}$ (blue circles), and the NQCRB (black solid line). The QCRB is identical to the SNL ($F_Q = N$), indicated by the dotted line. (b) $Q(\theta, \phi)$. For our state, $\hat{J}_n$ lies in the $x - z$ plane, so for definitiveness we chose $\hat{J}_n = \hat{J}_z$ (indicated by the thick blue line). (c-e): The probability distribution $P_m = |\langle m_j|\psi_1\rangle|^2$, where m_j is the mth eigenstate of $\hat{J}_j$, for $j = \{x, y, z\}$.